# P-Type Mn3O4 Nanosystems

Subjects: Nanoscience & Nanotechnology

Contributor: Chiara Maccato

Among oxide semiconductors, *p*-type $Mn_3O_4$ systems have been exploited in chemo-resistive sensors for various analytes, but their use in the detection of $H_2$, an important, though flammable, energy vector, has been scarcely investigated. Herein, we report for the first time on the plasma assisted-chemical vapor deposition (PA-CVD) of $Mn_3O_4$ nanomaterials, and on their on-top functionalization with Ag and $SnO_2$ by radio frequency (RF)-sputtering, followed by air annealing. The obtained $Mn_3O_4$-Ag and $Mn_3O_4$-$SnO_2$ nanocomposites were characterized by the occurrence of phase-pure tetragonal α-$Mn_3O_4$ (hausmannite) and a controlled Ag and $SnO_2$ dispersion. The system functional properties were tested towards $H_2$ sensing, yielding detection limits of 18 and 11 ppm for $Mn_3O_4$-Ag and $Mn_3O_4$-$SnO_2$ specimens, three orders of magnitude lower than the $H_2$ explosion threshold. These performances were accompanied by responses up to 25% to 500 ppm $H_2$ at 200 °C, superior to bare $Mn_3O_4$, and good selectivity against $CH_4$ and $CO_2$ as potential interferents. A rationale for the observed behavior, based upon the concurrence of built-in Schottky ($Mn_3O_4$/Ag) and *p-n* junctions ($Mn_3O_4$/$SnO_2$), and of a direct chemical interplay between the system components, is proposed to discuss the observed activity enhancement, which paves the way to the development of gas monitoring equipments for safety end-uses.

Mn3O4    Ag    SnO2    plasma assisted-chemical vapor deposition    hydrogen gas sensors

# 1. Introduction

The reliable detection of hazardous/flammable gases is of key importance in a variety of fields, encompassing disease diagnosis, environmental monitoring and human health protection [1][2][3][4][5][6]. In this broad scenario, a key role is played by the early recognition of molecular hydrogen ($H_2$), a zero-emission and clean fuel, with a high energy density of ≈130 MJ×$kg^{-1}$ [2][7], which has emerged as a future energy source for transportation, industrial and residential applications [8][9][10]. Nevertheless, since $H_2$ is colorless, odorless and highly flammable, the detection of hydrogen leakages at concentrations lower than hazardous levels [11][12][13][14] is extremely critical towards the emergence of a future hydrogen economy [7][8][15][16][17][18][19].

Simple architecture, cost-effective fabrication, stability under the operating conditions, and high efficiency, are the main requirements and core features of advanced sensors needed for such applications [16]. Among the various active systems and devices [20][21][22][23][24], metal oxide nanostructures have been the subject of an increasing interest, thanks to their high carrier mobility, easy fabrication and excellent stability [9][25][26][27][28]. In particular, whereas *n*-type oxide semiconductors have been largely investigated as gas sensors [8][9][12][15], *p*-type ones have not yet been widely studied [4][17][29][30], since their responses are typically lower than those of *n*-type systems with comparable morphology [31][32][33]. Nonetheless, *p*-type oxide semiconductors have an important potential as gas

sensors, and represent promising platforms for the development of devices exhibiting new functions [32], taking into account their appreciable activity as oxidation catalysts and the possibility of boosting their performances by tailoring their chemico-physical properties [2][31][34][35].

Among $p$-type systems, $Mn_3O_4$ has received significant attention due to its low cost, large natural abundance, environmentally friendly character and versatile chemico-physical properties, including the coexistence of mixed valence states [36][37]. Over the last decade, different studies have reported on $Mn_3O_4$-containing gas sensors for various analytes, including $CH_3CH_2OH$, $CH_3COCH_3$, $NH_3$ and chemical warfare agent simulants [31][35][36][37][38][39] [40][41]. Nonetheless, only two works on $Mn_3O_4$-based gas sensors for molecular hydrogen detection are available in the literature so far [35][42], and the implementation of $H_2$ sensors endowed with improved sensitivity and selectivity undoubtedly requires additional research efforts [29][35][37][38].

Beside tailoring the system morphology [25][26][33][39], a proficient way to enhance the functionality of bare $Mn_3O_4$ gas sensors involves their sensitization with suitable metal/oxide agents [8][18][35][42][43][44]. The ultimate aim of this strategy is the exploitation of synergistical chemical and electronic effects, in order to obtain improved performances at moderate working temperatures, an issue of key importance for the development of low power consumption devices [4][37][41]. In this context, the present study is devoted to the fabrication of $Mn_3O_4$-based chemo-resistive sensors for $H_2$ detection, sensitized through the on-top deposition of selected metal and metal oxide activators. As prototypes for the two categories, in this work our attention has been focused on the use of Ag, a potential catalyst promoting the reactions involved in the sensing process [45][46][47][48][49], and of $SnO_2$, by far one of the most investigated metal oxides for gas sensing applications, endowed with high electron mobility and gas sensitivity [10][13][25][26][50]. In particular, the occurrence of Schottky ($Mn_3O_4$/Ag) or $p$-$n$ ($Mn_3O_4$/$SnO_2$) junctions between the system components can indeed enhance the modulations of the space charge region, and of the measured electrical resistance, ultimately yielding improved sensing performances thanks to electronic effects [18] [26][33][43].

At variance with our previous studies, which have involved the fabrication of $Mn_3O_4$-based sensors by means of thermally activated chemical vapor deposition (CVD)-based processes [31][38][39][41], in this work a novel two-step plasma-assisted route was adopted for the preparation of the present materials. The fabrication procedure (Figure 1) involved: (i) the initial plasma assisted-CVD (PA-CVD) on alumina substrates of $MnO_2$ from $Mn(hfa)_2TMEDA$ (Hhfa = 1,1,1,5,5,5-hexafluoro-2,4-pentanedione; TMEDA = $N,N,N',N'$-tetramethylethylenediamine) [51][52], a molecular precursor never utilized so far for PA-CVD processes; (ii) the functionalization with Ag or $SnO_2$ by means of radio frequency (RF)-sputtering, and (iii) a final thermal treatment in air to trigger the transformation of $MnO_2$ into $Mn_3O_4$. The main focus of the present investigation was directed at elucidating the structural, compositional and morphological characteristics of the target materials and their interplay with the resulting sensing performances in hydrogen detection. The latter were investigated at a fixed humidity level as a function of the operating temperature, with particular regard to the role exerted by the formation of metal-oxide ($Mn_3O_4$/Ag) or oxide-oxide ($Mn_3O_4$/$SnO_2$) junctions. The obtained results indicate that the proposed preparation method yields $H_2$ sensors exhibiting favorable detection limits, promising responses at moderate temperature, as well as selectivity against

carbon dioxide and methane as potential interferents. To the best of our knowledge, this is the first report on hydrogen gas sensing by $Mn_3O_4$-based composites prepared by a plasma-assisted route.
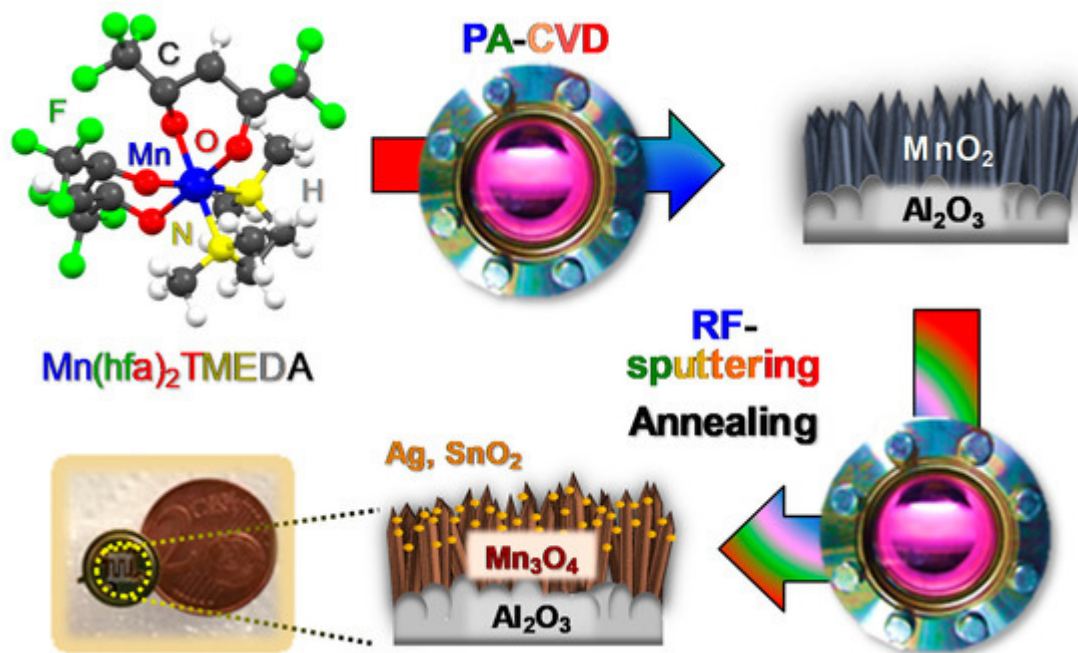


**Figure 1.** Scheme of the route proposed in the present study for the fabrication of $Mn_3O_4$-Ag and $Mn_3O_4$-$SnO_2$ nanomaterials.

# 2. Results and Discussion

## 2.1. Chemico-Physical Characterization

The fabrication process of the target materials is illustrated in Figure 1. Particular efforts were dedicated to elucidating the interplay between the adopted processing conditions and material chemical, physical and functional properties.

The system structure was investigated by XRD analyses (Figure 2). All the observed reflections located at $2\theta$ = 18.0°, 28.9°, 31.0°, 32.3° and 36.1° could be indexed to the (101), (112), (200), (103) and (211) planes of tetragonal hausmannite ($\alpha$-$Mn_3O_4$; $a$ = 5.762 Å and $c$ = 9.470 Å [31][38][53]). The occurrence of relatively weak and broad diffraction peaks suggested the formation of defective nanocrystallites [11], whose average dimensions were close to 25 nm for all the target specimens. A comparison of the signal relative intensities with those of the reference pattern [53] did not reveal any significant orientation/texturing effect, and no appreciable reflections from other Mn oxide polymorphs could be distinguished, highlighting the occurrence of phase-pure systems. Upon functionalization of $Mn_3O_4$ by RF-sputtering, no net variation in the recorded XRD patterns took place. The absence of noticeable diffraction peaks related to Ag or $SnO_2$ was traced back to their low content and high dispersion into the $Mn_3O_4$ systems [19][41][44][46] (see also XPS and SIMS results).
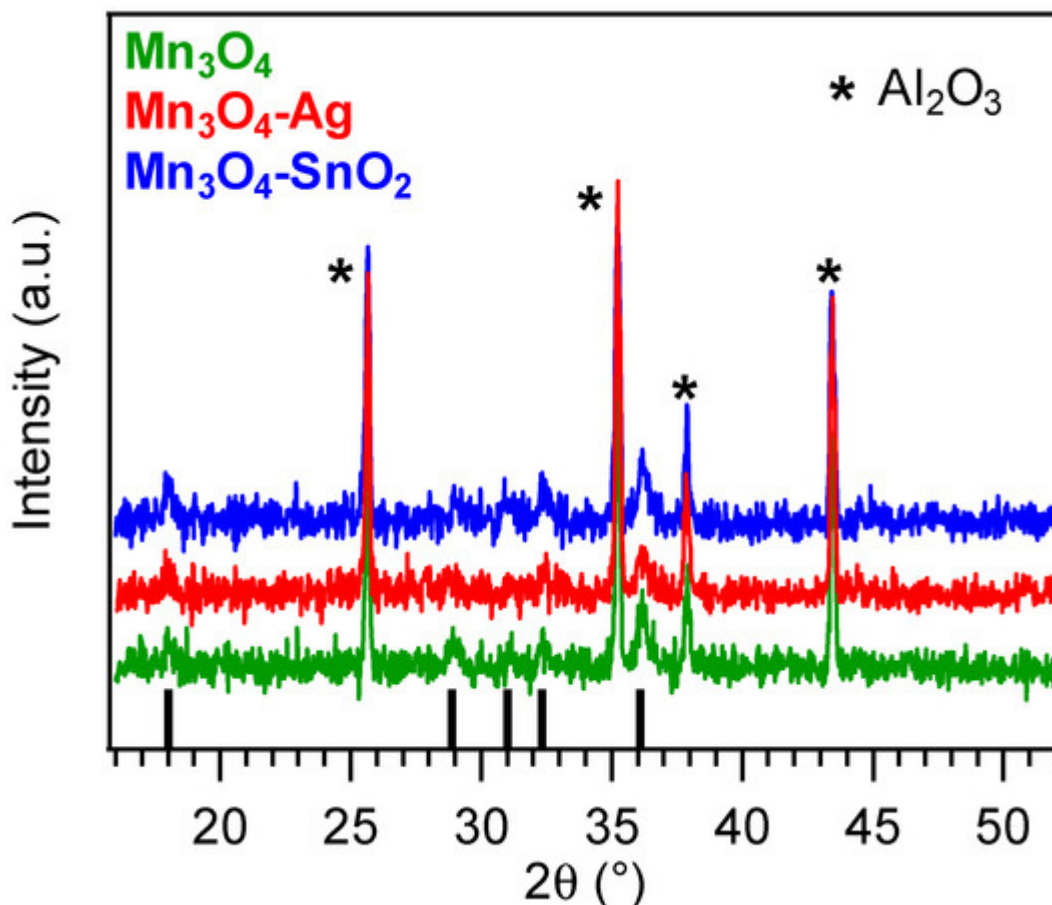
**Figure 2.** X-ray diffraction (XRD patterns for bare and functionalized $Mn_3O_4$ nanosystems. Vertical black bars correspond to α-$Mn_3O_4$ signals [53].

The surface chemical state of the developed materials was analyzed by means of XPS. Figure 3a displays the survey spectra for the target specimens, that revealed the presence of oxygen, manganese and eventually, silver or tin signals, for the functionalized systems, together with a minor carbon contribution (<10 at.%) resulting from adventitious contamination. The detection of manganese signals even after RF-sputtering suggested only a partial coverage of $Mn_3O_4$ by the deposited silver- and tin-containing species. Accordingly, Ag and Sn molar fractions were evaluated to be 47.0% and 31.0%, respectively. For bare $Mn_3O_4$, the $Mn2p_{3/2}$ component was located at BE = 641.8 eV (spin-orbit splitting (SOS) = 11.5 eV, Figure 3b), in accordance with previous literature data [31][35][38][41]. For the functionalized systems, a lower $Mn2p_{3/2}$ BE was observed (641.7 eV, for $Mn_3O_4$-Ag, and 641.5 eV, for $Mn_3O_4$-$SnO_2$). This finding suggested the formation of Schottky and *p-n* junctions for $Mn_3O_4$-Ag and $Mn_3O_4$-$SnO_2$, respectively [33][37][38][41][42], resulting in an Ag → $Mn_3O_4$ and $SnO_2$ → $Mn_3O_4$ electron transfer. This phenomenon, more pronounced for $SnO_2$-containing samples, as testified by the higher BE decrease, exerted a favorable influence on the resulting gas sensing performances. As regards silver (Figure 3c), the $Ag3d_{5/2}$ position (BE = 368.5 eV, SOS = 6.0 eV), as well as the pertaining Auger parameters (see also Figure S1; $α_1$ = 719.7 eV and $α_2$ = 725.6 eV), revealed a partial Ag surface oxidation, i.e., the coexistence of Ag(0) and Ag(I) oxide, as typically observed in similar cases [38][46][49][54]. Finally, the main tin photopeak (Figure 3d; BE($Sn3d_{5/2}$) = 486.9 eV; SOS = 8.4 eV) was located at higher energies than those reported for $SnO_2$ [14][55][56], in line with the above mentioned

charge transfer process. Taken together, these results highlighted the formation of nanocomposites in which the single components maintained their chemical identity, and enabled us to discard the formation of ternary phases, in line with XRD results. The deconvolution of O1s photopeaks (Figure S2) revealed the concurrence of two distinct bands at BE = 530.0 eV, resulting from lattice oxygen in $Mn_3O_4$, Ag(I) oxide ($Mn_3O_4$-Ag) or $SnO_2$ ($Mn_3O_4$-$SnO_2$) [14] [31][38][54][56], and 531.6 eV, assigned to oxygen species adsorbed on surface O defects [4][41][51][52][57]. The contribution of the latter component to the overall O1s signal increased from ≈36.0%, for bare $Mn_3O_4$, to ≈58.0%, for the functionalized specimens, indicating a parallel increase of the oxygen defect content. The latter feature had a direct beneficial impact on the resulting gas sensing behavior.
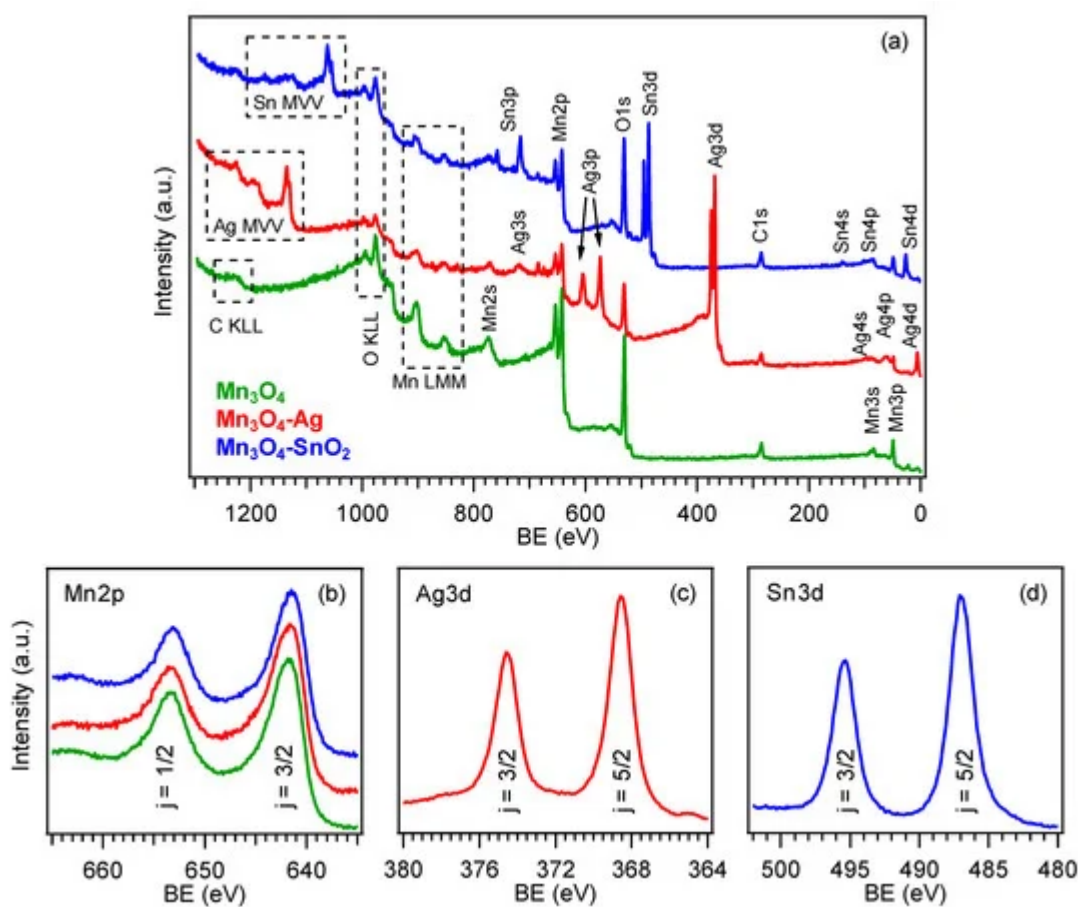


**Figure 3.** (**a**) X-ray photoelectron spectroscopy (XPS) wide-scan spectra pertaining to bare $Mn_3O_4$, $Mn_3O_4$-Ag and $Mn_3O_4$-$SnO_2$ samples. (**b**) Mn2p, (**c**) Ag3d and (**d**) Sn3d photoelectron peaks. The color code is reported in panel (**a**).

Complementary information on material chemical composition was obtained by SIMS in-depth profiling (Figure 4). Upon functionalization of $Mn_3O_4$, no significant variations in the overall deposit thickness took place (for all specimens, the average value was (400 ± 50) nm, as determined by cross-sectional FE-SEM analyses (see below and Figure 5)). The almost parallel trends of manganese and oxygen ionic yields suggested their common chemical origin, in line with the formation of phase-pure $Mn_3O_4$. Silver and tin trends could be described by an erfchian profile, such as in thermal diffusion processes [49]. For the $Mn_3O_4$-$SnO_2$ sample, Sn yield underwent a progressive decrease throughout the outer 100 nm, subsequently followed by a plateau, whereas, for the $Mn_3O_4$-

Ag specimen, the silver curve continuously declined even at higher depth values. In spite of these differences, a penetration of both Ag and Sn up to the interface with the alumina substrate was observed, and ascribed to the synergistical combination between the inherent RF-sputtering infiltration power and the $Mn_3O_4$ deposit open morphology [38][41][44][48] (see also Figure 5). This intimate contact between the system components is indeed an issue of key importance in order to benefit from their mutual electronic interplay, as discussed in detail below.
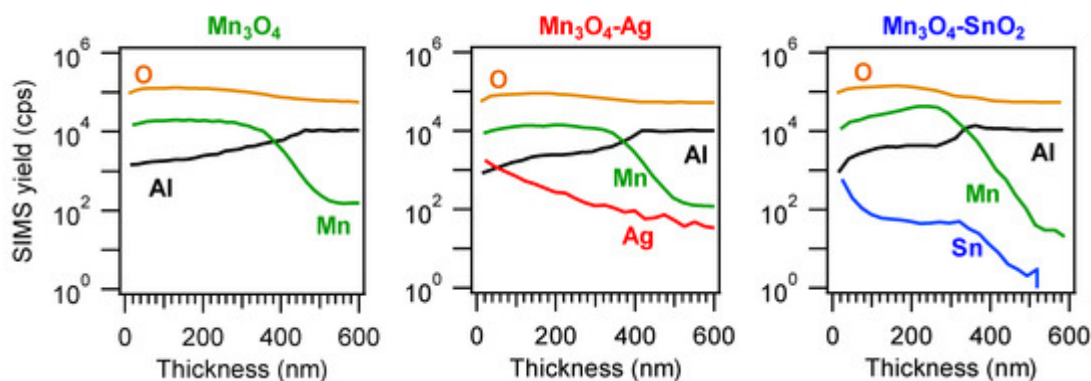


**Figure 4.** Secondary ion mass spectrometry (SIMS) depth profiles for $Mn_3O_4$, $Mn_3O_4$-Ag and $Mn_3O_4$-$SnO_2$ specimens.
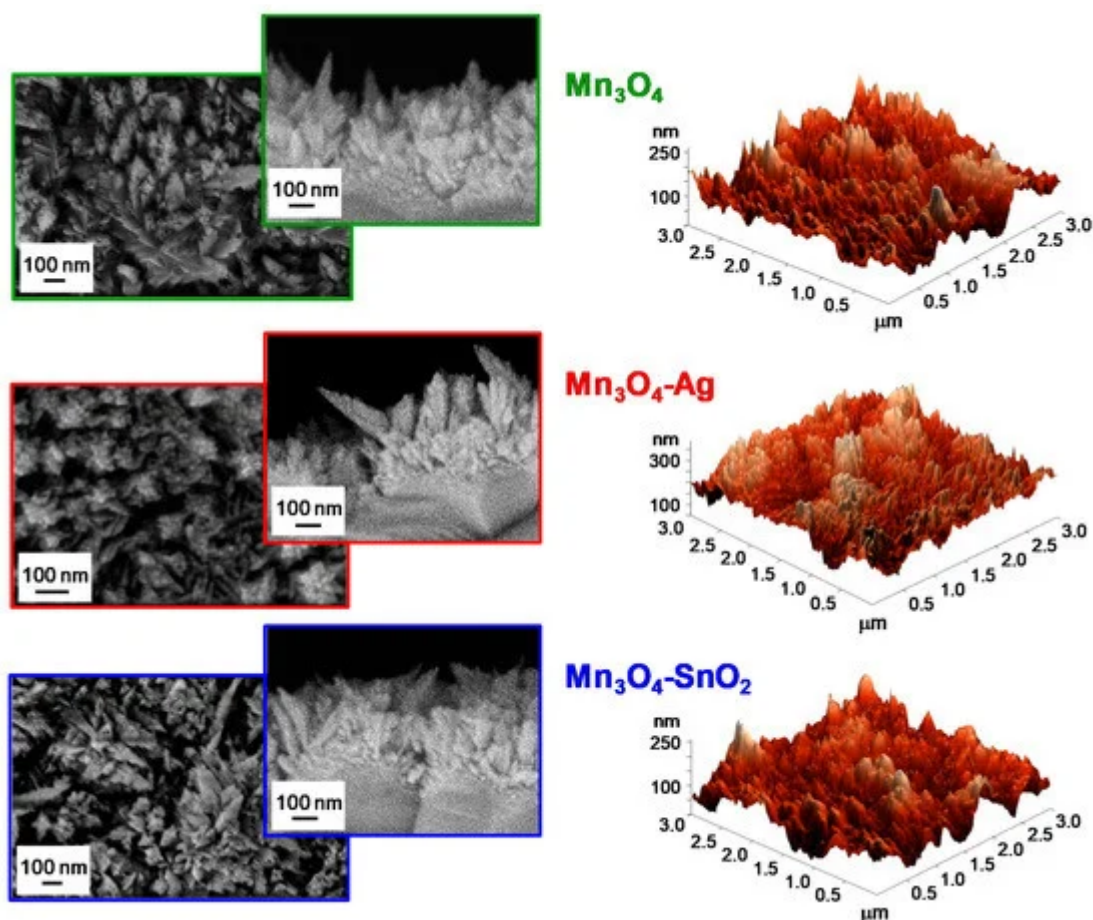


**Figure 5.** Representative plane-view and cross-sectional field emission-scanning electron microscopy (FE-SEM) micrographs (left panels) and atomic force microscopy (AFM) images (right panels) for $Mn_3O_4$, $Mn_3O_4$-Ag and

$Mn_3O_4$-$SnO_2$ samples.

The system morphology was investigated by the complementary use of FE-SEM and AFM. FE-SEM micrographs (see Figure 5, left side) highlighted that bare $Mn_3O_4$ was characterized by the presence of elongated nanoaggregates (mean size = 100 nm), whose interconnection resulted in the formation of arrays with an open morphology. This feature is indeed favorable in view of gas sensing applications, since a higher area available for the interaction with the surrounding gases has a beneficial effect on the ultimate material functional performances [15][19][25][31][40]. After Ag and $SnO_2$ introduction, no marked variations involving aggregate coalescence/collapse could be observed, validating the potential of the adopted synthetic route in functionalizing $Mn_3O_4$ nano-deposits without any undesired morphological alteration. AFM analyses (Figure 5, right side) confirmed the presence of the aforementioned aggregates uniformly protruding from the growth substrate, resulting in a crack-free and homogeneous granular topography, yielding an average RMS surface roughness of 40 nm for all the analyzed specimens.

## 2.2. Gas Sensing Performances

Figure 6 displays representative dynamical responses of the developed sensors towards square concentration pulses of gaseous hydrogen. All the target materials exhibited a *p*-type sensing behavior, as indicated by the resistance increase upon $H_2$ exposure due to the reaction of the analyte with adsorbed oxygen species, resulting in a decrease of the major *p*-type carrier concentration [2][16][31][35][39]. This phenomenon is in agreement with the fact that $Mn_3O_4$ is the main system component, as indicated by structural and compositional characterization [44].
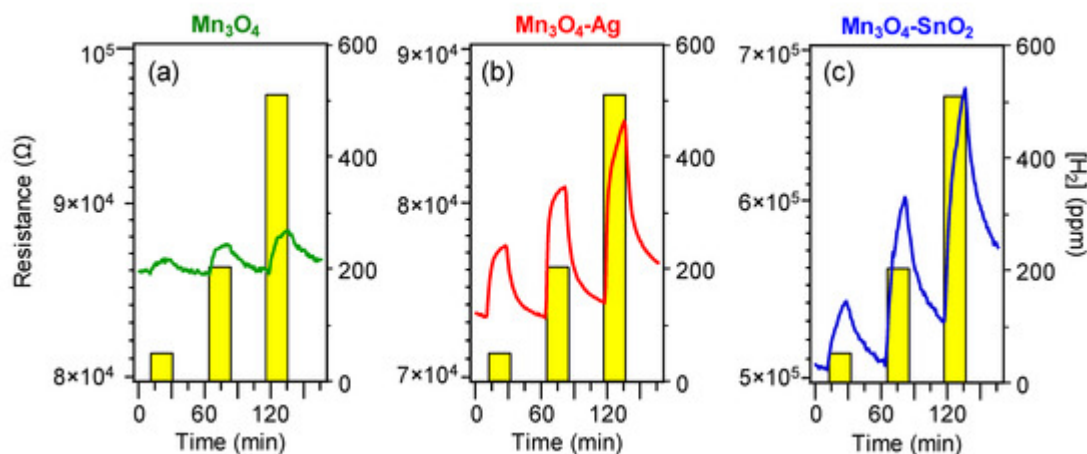


**Figure 6.** Dynamical responses of $Mn_3O_4$ (**a**), $Mn_3O_4$-Ag (**b**) and $Mn_3O_4$-$SnO_2$ (**c**) nanosystems vs. different $H_2$ concentrations, at a fixed working temperature of 200 °C.

Remarkably, data in Figure 6 evidence that the on-top deposition of Ag and $SnO_2$ was an effective mean to increase the electrical property modulation upon $H_2$ exposure with respect to pure $Mn_3O_4$. For both composite systems, the measured resistance underwent a relatively sharp rise upon hydrogen exposure, and a subsequent slower increase up to the end of each gas pulse. This phenomenon suggested that the rate-limiting step in the resistance change was the chemisorption of molecular hydrogen on the sensor surface [15][31][41][48]. In spite of an

incomplete baseline recovery after switching off hydrogen pulses, the measured resistance variations were almost proportional to the used hydrogen concentrations, enabling us to rule out significant saturation effects, an important starting point for eventual practical applications [15][38][39].

To account for the performance increase yielded by composite systems, it is necessary to consider the mechanism of hydrogen detection by the target $p$-type materials, which can be described as follows. Upon air exposure prior to contact with the target analyte, oxygen molecules undergo chemisorption processes, yielding the formation of various species [6][9][29][36][43][57], among which $O^-$ is the prevailing one in the present working temperature interval [14][17][30][33]:

$$O_{2\ (g)} \rightleftarrows 2O^-_{\ (ads)} + 2h^+ \quad (3)$$

As a consequence, the formation of a low resistance hole accumulation layer (HAL) in the near surface $Mn_3O_4$ region takes place (Figure 7; HAL thickness = 20.6 nm, see the Supporting Information) [32][33][37][47]. The subsequent analyte chemisorption is accompanied by electron injection into the system conduction band [3][4][7][29][40][44][58]:

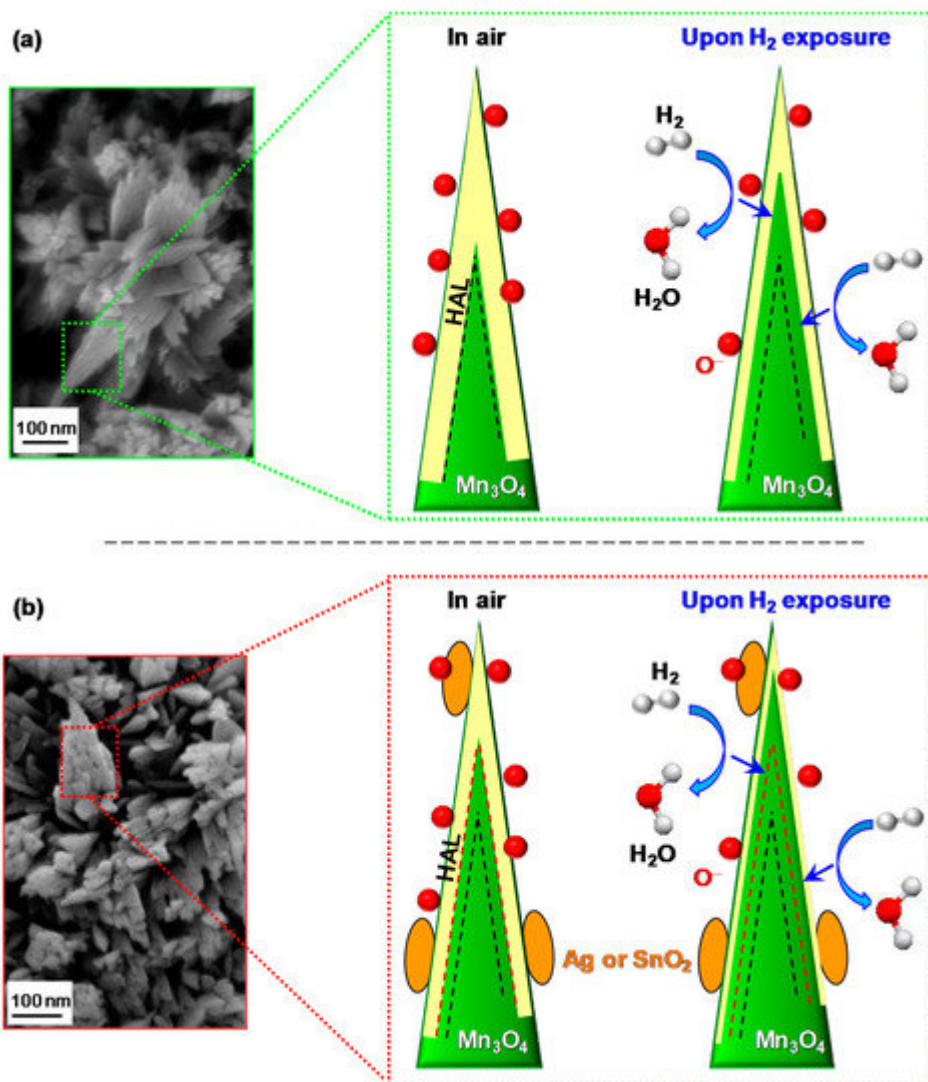$$H_{2\ (ads)} + O^-_{\ (ads)} \rightleftarrows H_2O_{\ (g)} + e^- \quad (4)$$
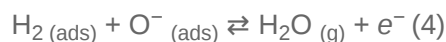
**Figure 7.** Schematics of the hydrogen gas sensing mechanism and corresponding hole accumulation layer (HAL) modulation for nanosystems based on: (**a**) bare $Mn_3O_4$; (**b**) functionalized $Mn_3O_4$. The dashed black and red lines indicate the HAL boundaries in air in case of bare and functionalized $Mn_3O_4$, respectively. Red spheres, yellow areas, and orange ovals indicate adsorbed oxygen, HAL thickness, and functionalizing agent (Ag or $SnO_2$), respectively. Blue arrows indicate electron flow due to $H_2$ oxidation (see reaction 4).

A process which decreases the hole concentration and the HAL thickness, resulting, in turn, in an increase of the measured resistance [5][16][17][18][42][43]. Finally, upon switching off the gas pulse, the sensor surface is again in contact with air, and the original situation is restored, with a recovery of the pristine HAL width [30][31][41].

Since all the investigated systems have almost identical mean crystallite dimensions, grain size and RMS roughness values, a significant influence of these parameters on the different gas sensing performances can be reasonably ruled out. Indeed, the enhanced responses of composite sensors with respect to the pristine $Mn_3O_4$ can be first explained in terms of electronic effects occurring at the interface between $Mn_3O_4$ and the functionalizing agents, a key aspect to be considered for a deep understanding of gas sensing phenomena [26].

For $Mn_3O_4$-Ag sensors, these processes result from the formation of $Mn_3O_4$/Ag Schottky junctions, whose occurrence produces a Ag → $Mn_3O_4$ electron flow [38][59] (see also the above XPS data), and a consequent thinning of the HAL width in comparison with bare $Mn_3O_4$ (compare Figure 7a,b). As a consequence, HAL variations upon contact of the sensor with gaseous $H_2$ produce higher responses by increasing the registered resistance modulations [38][44]. An analogous phenomenon occurs for $Mn_3O_4$-$SnO_2$ systems (Figure 7b; HAL thickness = 12.4 nm, see the Supporting Information), although in this case the $SnO_2$ → $Mn_3O_4$ electron flow is triggered by a different phenomenon, i.e., the presence of _p-n_ $Mn_3O_4$/$SnO_2$ junctions [32][33][37][41][42][43][45].

The latter effect can, in principle, result in enhanced variations of the HAL extension with respect to the case of $Mn_3O_4$-Ag sensors, since the occurrence of a partial silver oxidation (as evidenced by XPS analysis, see above) precludes a full exploitation of electron transfer effects resulting from the establishment of $Mn_3O_4$/Ag Schottky junctions [38][46].

Nonetheless, the enhanced hydrogen detection efficiency of $Mn_3O_4$-based nanocomposites with respect to bare manganese oxide is likely due to the concurrence of additional cooperative phenomena. For both $Mn_3O_4$-Ag and $Mn_3O_4$-$SnO_2$ systems, the higher content of oxygen defects at the composite surface with respect to bare $Mn_3O_4$ (see the above XPS data and Figure S2), as well as the exposure of a high density of heterointerfaces, can in fact supply active sites for a more efficient chemisorption of both oxygen and analyte molecules, which, in turn, boosts the resulting gas responses [4][8][16][17][18][30][43]. In addition, the intimate component contact enabled by the adopted preparation route, yielding a good intergranular coupling, enables a proficient exploitation of their chemical interplay [38][44][48], related to the synergistical combination of materials with different catalytic activities [10][27][37][41][47]. Hence, the improved sensing performances of functionalized $Mn_3O_4$ systems can be related to the concomitance of electronic and catalytic effects.

Taken together, the above observations can account for the improved performances at lower working temperatures of $SnO_2$-containing systems with respect to Ag-containing ones. This result is exemplified by an inspection of Figure 8, showing that, apart from the appreciable response enhancement, deposition of Ag and $SnO_2$ onto $Mn_3O_4$ resulted in different trends as a function of the operating temperature. In the case of $Mn_3O_4$-Ag sensors, the progressive response rise indicated an enhanced extent of reaction (4) upon increasing the thermal energy supply [2][8][15][31][38][39]. Conversely, as concerns $Mn_3O_4$-$SnO_2$, a maximum-like response behavior was observed, the best operating temperature being 200 °C. Such a response trend, in line with previous reports regarding $H_2$ detection by other metal oxides [7][9][17][19][29][43][60], suggested the occurrence of a steady equilibrium between hydrogen adsorption and desorption at 200 °C, whereas an increase of the working temperature resulted in a predominant analyte desorption [27][33][57][60][61]. The lower value of the optimum operating temperature for $Mn_3O_4$-$SnO_2$ in comparison to $Mn_3O_4$-Ag is in line with the more efficient $SnO_2$ → $Mn_3O_4$ electron transfer (see the above XPS data).
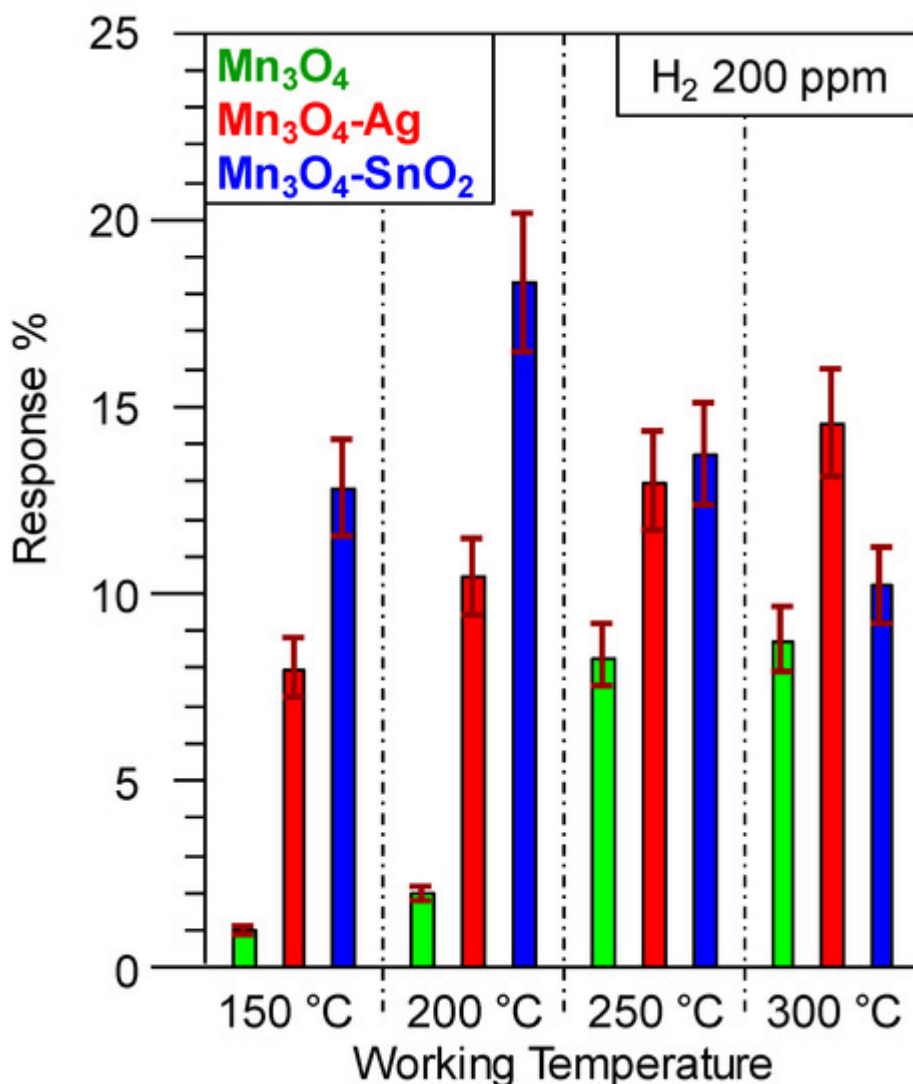
**Figure 8.** Gas responses to a fixed $H_2$ concentration (200 ppm) for the target $Mn_3O_4$-based sensors at different working temperatures.

The potential of the present results is highlighted by the fact that the best $H_2$ responses obtained for $Mn_3O_4$-Ag (at 300 °C) and $Mn_3O_4$-$SnO_2$ (at 200 °C) were higher than those reported for sensors based not only on $Mn_3O_4$ [35][42], but even on other *p*-type oxides, including CuO [3][29], NiO [2][30], $BiFeO_3$ [7], $Co_3O_4$ [16][19], $Ni_xCo_{3-x}O_4$ [16], as well as nanocomposites based on CuO-Pt [4] and CuO-$WO_3$ [18]. In addition, the same responses compared favorably with those pertaining to various $MnO_2$-based nanomaterials/thin films in the detection of the same analyte [1][60][61]. A comparison of selected representative data is reported in Table S1. It is also worthwhile highlighting that the optimal operating temperature for $H_2$ detection by the present materials (200 °C for $Mn_3O_4$-$SnO_2$ systems) was lower than the ones reported for $Mn_3O_4$ [35], $MnO_2$ [8], CuO [3][17][29], $Co_3O_4$ [16], NiO [9], NiO-ZnO [43], $Ni_xCo_{3-x}O_4$ [16], $BiFeO_3$ [7] and CuO-$WO_3$ sensors [18]. This result is of importance, not only to avoid dangerous temperature-triggered explosions, but also to implement sensing devices with a higher service life and a lower power consumption [11][25][38][41].

Gas responses were also analyzed as a function of $H_2$ concentration (Figure S3). The obtained linear trends in the log-log scale confirmed the absence of appreciable saturation phenomena, an important prerequisite for a quantitative analyte detection [37][38][39][44][48]. The best detection limits obtained by fitting experimental data with equation (2) ((18 ± 1) ppm and (11 ± 1) ppm for $Mn_3O_4$-Ag and $Mn_3O_4$-$SnO_2$ sensors, respectively) were close to those previously reported for $MnO_2$ [8], CoO [6] and CuO-$TiO_2$-Au [44] sensors, and inferior than those pertaining to ZnO ones [15]. It is also worth noticing that these values were nearly three orders of magnitude lower than the $H_2$ lower explosion limit (LEL, 40000 ppm) [2][11][12][23][43], highlighting thus the detection efficiency of the present systems.

Beyond sensitivity, selectivity is an important parameter for the eventual utilization of gas sensing devices [6][11][19] [27][30]. The responses towards a specific test gas are in fact required to be higher than those of other potential interferents, in order to avoid false alarms in real-time gas monitoring equipment [36][38][39]. In particular, the choice of $CH_4$ and $CO_2$ as potential interferents in real-time hydrogen leak detection is motivated by the fact that: (i) hydrogen and methane are common reducing gases, either stored, or used together [1][13]; (ii) the presence of carbon dioxide may hamper hydrogen recognition [5][21][43] in the case of fuel cells eliminating $CO_2$ and producing electricity and $H_2$ [62]. As shown in Figure S4, the present sensors yielded no responses towards $CO_2$, and only weak signals upon exposure to $CH_4$. In the latter case, the selectivity was estimated as the ratio between the responses to $H_2$ and $CH_4$ [32][41], yielding values of 22 and 24 for $Mn_3O_4$-Ag and $Mn_3O_4$-$SnO_2$ at the best working temperatures (300 and 200 °C, respectively). Though preliminary in nature, the latter results are an attractive starting point for further studies aimed at implementing exclusive $H_2$ sensors, which are highly required for practical applications [13].

# References

1. Zöpfl, A.; Lemberger, M.-M.; König, M.; Ruhl, G.; Matysik, F.-M.; Hirsch, T. Reduced graphene oxide and graphene composite materials for improved gas sensing at low temperature. Faraday Discuss. 2014, 173, 403–414.

2. Stamataki, M.; Tsamakis, D.; Brilis, N.; Fasaki, I.; Giannoudakos, A.; Kompitsas, M. Hydrogen gas sensors based on PLD grown NiO thin film structures. Phys. Status Solidi 2008, 205, 2064–2068.

3. Duc, L.D.; Le, D.T.T.; Duy, N.V.; Hoa, N.D.; Hieu, N.V. Single crystal cupric oxide nanowires: Length- and density-controlled growth and gas-sensing characteristics. Physica E 2014, 58, 16–23.

4. Sarıca, N.; Alev, O.; Arslan, L.Ç.; Öztürk, Z.Z. Characterization and gas sensing performances of noble metals decorated CuO nanorods. Thin Solid Film. 2019, 685, 321–328.

5. Tonezzer, M.; Le, D.T.T.; Iannotta, S.; Hieu, N.V. Selective discrimination of hazardous gases using one single metal oxide resistive sensor. Sens. Actuators B 2018, 277, 121–128.

6. Li, L.H.; Xiao, J.; Yang, G.W. Amorphization of cobalt monoxide nanocrystals and related explosive gas sensing applications. Nanotechnology 2015, 26, 415501.

7. Bala, A.; Majumder, S.B.; Dewan, M.; Roy Chaudhuri, A. Hydrogen sensing characteristics of perovskite based calcium doped BiFeO3 thin films. Int. J. Hydrogen Energy 2019, 44, 18648–18656.

8. Sanger, A.; Kumar, A.; Kumar, A.; Chandra, R. Highly sensitive and selective hydrogen gas sensor using sputtered grown Pd decorated MnO2 nanowalls. Sens. Actuators B 2016, 234, 8–14.

9. Kaur, N.; Comini, E.; Zappa, D.; Poli, N.; Sberveglieri, G. Nickel oxide nanowires: Vapor liquid solid synthesis and integration into a gas sensing device. Nanotechnology 2016, 27, 205701.

10. Lu, Z.; Zhou, Q.; Xu, L.; Gui, Y.; Zhao, Z.; Tang, C.; Chen, W. Synthesis and characterization of highly sensitive hydrogen (H2) sensing device based on Ag doped SnO2 nanospheres. Materials 2018, 11, 492.

11. Tian, X.Q.; Yang, L.; Qing, X.X.; Yu, K.; Wang, X.F. Trace level detection of hydrogen gas using birnessite-type manganese oxide. Sens. Actuators B 2015, 207, 34–42.

12. Lee, Y.T.; Lee, J.M.; Kim, Y.J.; Joe, J.H.; Lee, W. Hydrogen gas sensing properties of PdO thin films with nano-sized cracks. Nanotechnology 2010, 21, 165503.

13. Huang, H.; Gong, H.; Chow, C.L.; Guo, J.; White, T.J.; Tse, M.S.; Tan, O.K. Low-temperature growth of SnO2 nanorod arrays and tunable n–p–n sensing response of a ZnO/SnO2 heterojunction for exclusive hydrogen sensors. Adv. Funct. Mater. 2011, 21, 2680–2686.

14. Bigiani, L.; Zappa, D.; Maccato, C.; Comini, E.; Barreca, D.; Gasparotto, A. Quasi-1D MnO2 nanocomposites as gas sensors for hazardous chemicals. Appl. Surf. Sci. 2020, 512, 145667.

15. Barreca, D.; Bekermann, D.; Comini, E.; Devi, A.; Fischer, R.A.; Gasparotto, A.; Maccato, C.; Sberveglieri, G.; Tondello, E. 1D ZnO nano-assemblies by plasma-CVD as chemical sensors for flammable and toxic gases. Sens. Actuators B 2010, 149, 1–7.

16. Govindhan, M.; Sidhureddy, B.; Chen, A. High-temperature hydrogen gas sensor based on three-dimensional hierarchical-nanostructured nickel–cobalt oxide. ACS Appl. Nano Mater. 2018, 1, 6005–6014.

17. Choi, Y.-H.; Kim, D.-H.; Hong, S.-H.; Hong, K.S. H2 and C2H5OH sensing characteristics of mesoporous p-type CuO films prepared via a novel precursor-based ink solution route. Sens. Actuators B 2013, 178, 395–403.

18. Haviar, S.; Čapek, J.; Batková, Š.; Kumar, N.; Dvořák, F.; Duchoň, T.; Fialová, M.; Zeman, P. Hydrogen gas sensing properties of WO3 sputter-deposited thin films enhanced by on-top deposited CuO nanoclusters. Int. J. Hydrogen Energy 2018, 43, 22756–22764.

19. Barreca, D.; Comini, E.; Gasparotto, A.; Maccato, C.; Pozza, A.; Sada, C.; Sberveglieri, G.; Tondello, E. Vapor phase synthesis, characterization and gas sensing performances of Co3O4 and Au/Co3O4 nanosystems. J. Nanosci. Nanotechnol. 2010, 10, 8054–8061.

20. Fortunato, E.; Malik, A.; Martins, R. Photochemical sensors based on amorphous silicon thin films. Sens. Actuators B 1998, 46, 202–207.

21. Hashtroudi, H.; Atkin, P.; Mackinnon, I.D.R.; Shafiei, M. Low-operating temperature resistive nanostructured hydrogen sensors. Int. J. Hydrogen Energy 2019, 44, 26646–26664.

22. Hübert, T.; Boon-Brett, L.; Black, G.; Banach, U. Hydrogen sensors—A review. Sens. Actuators B 2011, 157, 329–352.

23. Penner, R.M. A nose for hydrogen gas: Fast, sensitive H2 sensors using electrodeposited nanomaterials. Acc. Chem. Res. 2017, 50, 1902–1910.

24. Meng, X.; Zhang, Q.; Zhang, S.; He, Z. The enhanced H2 selectivity of SnO2 gas sensors with the deposited SiO2 filters on surface of the sensors. Sensors 2019, 19, 2478.

25. Comini, E.; Baratto, C.; Concina, I.; Faglia, G.; Falasconi, M.; Ferroni, M.; Galstyan, V.; Gobbi, E.; Ponzoni, A.; Vomiero, A.; et al. Metal oxide nanoscience and nanotechnology for chemical sensors. Sens. Actuators B 2013, 179, 3–20.

26. Zappa, D.; Galstyan, V.; Kaur, N.; Munasinghe Arachchige, H.M.M.; Sisman, O.; Comini, E. "Metal oxide -based heterostructures for gas sensors"—A review. Anal. Chim. Acta 2018, 1039, 1–23.

27. Yang, Y.; Wang, X.; Yi, G.; Li, H.; Shi, C.; Sun, G.; Zhang, Z. Hydrothermal synthesis of Co3O4/ZnO hybrid nanoparticles for triethylamine detection. Nanomaterials 2019, 9, 1599.

28. Coll, M.; Fontcuberta, J.; Althammer, M.; Bibes, M.; Boschker, H.; Calleja, A.; Cheng, G.; Cuoco, M.; Dittmann, R.; Dkhil, B.; et al. Towards oxide electronics: A roadmap. Appl. Surf. Sci. 2019, 482, 1–93.

29. Hoa, N.D.; An, S.Y.; Dung, N.Q.; Van Quy, N.; Kim, D. Synthesis of p-type semiconducting cupric oxide thin films and their application to hydrogen detection. Sens. Actuators B 2010, 146, 239–244.

30. Zhao, S.; Shen, Y.; Zhou, P.; Zhang, J.; Zhang, W.; Chen, X.; Wei, D.; Fang, P.; Shen, Y. Highly selective NO2 sensor based on p-type nanocrystalline NiO thin films prepared by sol–gel dip coating. Ceram. Int. 2018, 44, 753–759.

31. Bigiani, L.; Maccato, C.; Carraro, G.; Gasparotto, A.; Sada, C.; Comini, E.; Barreca, D. Tailoring vapor-phase fabrication of Mn3O4 nanosystems: From synthesis to gas-sensing applications. ACS Appl. Nano Mater. 2018, 1, 2962–2970.

32. Kim, H.-J.; Lee, J.-H. Highly sensitive and selective gas sensors using p-type oxide semiconductors: Overview. Sens. Actuators B 2014, 192, 607–627.

33. Kim, J.-H.; Lee, J.-H.; Mirzaei, A.; Kim, H.W.; Kim, S.S. SnO2 (n)-NiO (p) composite nanowebs: Gas sensing properties and sensing mechanisms. Sens. Actuators B 2018, 258, 204–214.

34. Chen, Z.; Jiao, Z.; Pan, D.; Li, Z.; Wu, M.; Shek, C.-H.; Wu, C.M.L.; Lai, J.K.L. Recent advances in manganese oxide nanocrystals: Fabrication, characterization, and microstructure. Chem. Rev. 2012, 112, 3833–3855.

35. Na, C.W.; Park, S.-Y.; Chung, J.-H.; Lee, J.-H. Transformation of ZnO nanobelts into single-crystalline Mn3O4 nanowires. ACS Appl. Mater. Interfaces 2012, 4, 6565–6572.

36. John, N.; Thomas, P.; Divya, K.V.; Abraham, K.E. Enhanced room temperature gas sensing of aligned Mn3O4 nanorod assemblies functionalized by aluminum anodic membranes. Nanotechnology 2018, 29, 335503.

37. Zhou, T.; Liu, X.; Zhang, R.; Wang, L.; Zhang, T. Constructing hierarchical heterostructured Mn3O4/Zn2SnO4 materials for efficient gas sensing reaction. Adv. Mater. Interfaces 2018, 5, 1800115.

38. Bigiani, L.; Zappa, D.; Barreca, D.; Gasparotto, A.; Sada, C.; Tabacchi, G.; Fois, E.; Comini, E.; Maccato, C. Sensing nitrogen mustard gas simulant at the ppb scale via selective dual-site activation at Au/Mn3O4 interfaces. ACS Appl. Mater. Interfaces 2019, 11, 23692–23700.

39. Maccato, C.; Bigiani, L.; Carraro, G.; Gasparotto, A.; Sada, C.; Comini, E.; Barreca, D. Toward the detection of poisonous chemicals and warfare agents by functional Mn3O4 nanosystems. ACS Appl. Mater. Interfaces 2018, 10, 12305–12310.

40. Ben Said, L.; Inoubli, A.; Bouricha, B.; Amlouk, M. High Zr doping effects on the microstructural and optical properties of Mn3O4 thin films along with ethanol sensing. Spectrochim. Acta Part A 2017, 171, 487–498.

41. Bigiani, L.; Zappa, D.; Maccato, C.; Gasparotto, A.; Sada, C.; Comini, E.; Barreca, D. Mn3O4 nanomaterials functionalized with Fe2O3 and ZnO: Fabrication, characterization, and ammonia sensing properties. Adv. Mater. Interfaces 2019, 6, 1901239.

42. Kim, H.W.; Kwon, Y.J.; Na, H.G.; Cho, H.Y.; Lee, C.; Jung, J.H. One-pot synthesis of Mn3O4-decorated GaN nanowires for drastic changes in magnetic and gas-sensing properties. Microelectron. Eng. 2015, 139, 60–69.

43. Nakate, U.T.; Ahmad, R.; Patil, P.; Wang, Y.; Bhat, K.S.; Mahmoudi, T.; Yu, Y.T.; Suh, E.-K.; Hahn, Y.-B. Improved selectivity and low concentration hydrogen gas sensor application of Pd sensitized heterojunction n-ZnO/p-NiO nanostructures. J. Alloy. Compd. 2019, 797, 456–464.

44. Barreca, D.; Carraro, G.; Comini, E.; Gasparotto, A.; Maccato, C.; Sada, C.; Sberveglieri, G.; Tondello, E. Novel synthesis and gas sensing performances of CuO–TiO2 nanocomposites functionalized with Au nanoparticles. J. Phys. Chem. C 2011, 115, 10510–10517.

45. Acharyya, S.S.; Ghosh, S.; Sharma, S.K.; Bal, R. Fabrication of Ag nanoparticles supported on one-dimensional (1D) Mn3O4 spinel nanorods for selective oxidation of cyclohexane at room temperature. New J. Chem. 2016, 40, 3812–3820.

46. Carraro, G.; Gasparotto, A.; Maccato, C.; Gombac, V.; Rossi, F.; Montini, T.; Peeters, D.; Bontempi, E.; Sada, C.; Barreca, D.; et al. Solar H2 generation via ethanol photoreforming on ε-Fe2O3 nanorod arrays activated by Ag and Au nanoparticles. RSC Adv. 2014, 4, 32174–32179.

47. Rahaman, H.; Kundu, S.; Ghosh, S.K. Size-selective silver-induced evolution of Mn3O4-Ag nanocomposites for effective ethanol sensing. ChemistrySelect 2017, 2, 6991–6999.

48. Simon, Q.; Barreca, D.; Gasparotto, A.; Maccato, C.; Tondello, E.; Sada, C.; Comini, E.; Devi, A.; Fischer, R.A. Ag/ZnO nanomaterials as high performance sensors for flammable and toxic gases. Nanotechnology 2012, 23, 025502.

49. Carraro, G.; Barreca, D.; Comini, E.; Gasparotto, A.; Maccato, C.; Sada, C.; Sberveglieri, G. Controlled synthesis and properties of β-Fe2O3 nanosystems functionalized with Ag or Pt nanoparticles. CrystEngComm 2012, 14, 6469–6476.

50. Rahman, M.M.; Alam, M.M.; Asiri, A.M. Fabrication of an acetone sensor based on facile ternary MnO2/Gd2O3/SnO2 nanosheets for environmental safety. New J. Chem. 2017, 41, 9938–9946.

51. Barreca, D.; Carraro, G.; Fois, E.; Gasparotto, A.; Gri, F.; Seraglia, R.; Wilken, M.; Venzo, A.; Devi, A.; Tabacchi, G.; et al. Manganese(II) molecular sources for plasma-assisted CVD of Mn oxides and fluorides: From precursors to growth process. J. Phys. Chem. C 2018, 122, 1367–1375.

52. Maccato, C.; Bigiani, L.; Carraro, G.; Gasparotto, A.; Seraglia, R.; Kim, J.; Devi, A.; Tabacchi, G.; Fois, E.; Pace, G.; et al. Molecular engineering of MnII diamine diketonate precursors for the vapor deposition of manganese oxide nanostructures. Chem. Eur. J. 2017, 23, 17954–17963.

53. JCPDS card no. 024-0734 (2000).

54. Bigiani, L.; Barreca, D.; Gasparotto, A.; Maccato, C. Mn3O4 thin films functionalized with Ag, Au, and TiO2 analyzed using X-ray photoelectron spectroscopy. Surf. Sci. Spectra 2018, 25, 014003.

55. Briggs, D.; Seah, M.P. Practical Surface Analysis: Auger and X-ray Photoelectron Spectroscopy, 2nd ed.; John Wiley & Sons: Hoboken, NJ, USA, 1990.

56. NIST X-ray Photoelectron Spectroscopy Database. Available online: http://srdata.nist.gov/xps (accessed on 31 December 2019).

57. Liu, H.; Wang, F.; Hu, K.; Zhang, B.; He, L.; Zhou, Q. Superior hydrogen sensing property of porous NiO/SnO2 nanofibers synthesized via carbonization. Nanomaterials 2019, 9, 1250.

58. Sharma, J.K.; Srivastava, P.; Ameen, S.; Akhtar, M.S.; Singh, G.; Yadava, S. Azadirachta Indica plant-assisted green synthesis of Mn3O4 nanoparticles: Excellent thermal catalytic performance

and chemical sensing behavior. J. Colloid Interface Sci. 2016, 472, 220–228.

59. Zhang, Z.; Yates, J.T. Band bending in semiconductors: Chemical and physical consequences at surfaces and interfaces. Chem. Rev. 2012, 112, 5520–5551.

60. Zhang, C.; Boudiba, A.; Navio, C.; Olivier, M.-G.; Snyders, R.; Debliquy, M. Study of selectivity of NO2 sensors composed of WO3 and MnO2 thin films grown by radio frequency sputtering. Sens. Actuators B 2012, 161, 914–922.

61. Jung, D.; Yoon, Y.; Lee, G.S. Hydrogen sensing characteristics of carbon-nanotube sheet decorated with manganese oxides. Chem. Phys. Lett. 2013, 577, 96–101.

62. Fuel Cell-Based System Converts Atmospheric CO2 into Usable Electric Current. Available online: https://www.theengineer.co.uk/fuel-cell-based-system-co2/ (accessed on 31 December 2019).